Non-dimensional energy dissipation rate near the turbulent/non-turbulent interfacial layer in free shear flows and shear free turbulence

Tomoaki Watanabe[1]†, Carlos B. da Silva[2] and Koji Nagata[1]

[1]Department of Aerospace Engineering, Nagoya University, Nagoya 464-8603, Japan
[2]Instituto Superior Técnico, Universidade de Lisboa, Lisboa 1049-001, Portugal

(Received xx; revised xx; accepted xx)

The non-dimensional dissipation rate $C_\varepsilon = \varepsilon L/u'^3$, where ε, L and u' are the viscous energy dissipation rate, integral length scale of turbulence and root-mean-square of the velocity fluctuations, respectively, is computed and analysed within the turbulent/non-turbulent interfacial (TNTI) layer using direct numerical simulations of planar jet, mixing layer and shear free turbulence. The TNTI layer that separates the turbulent and non-turbulent regions exists at the edge of free shear turbulent flows and turbulent boundary layers, and comprises both viscous superlayer and turbulent sublayer regions. The computation of C_ε is made possible by the introduction of an original procedure, based on local volume averages within spheres of radius r, combined with the conditional sampling as a function of the location with respective to the TNTI layer. The new procedure based on local volume averages allows a detailed investigation of the scale dependence of several turbulent quantities near the TNTI layer. An important achievement of this procedure consists in permitting to compute the turbulent integral scale within the TNTI layer, which is shown to be approximately constant. Both non-dimensional dissipation rate and turbulent Reynolds number Re_λ vary in space within the TNTI layer, where two relations are observed: $C_\varepsilon \sim Re_\lambda^{-1}$ and $C_\varepsilon \sim Re_\lambda^{-2}$. Specifically, whereas in the viscous superlayer and part of the turbulent sublayer display $C_\varepsilon \sim Re_\lambda^{-2}$, the remaining of the turbulent sublayer exhibits $C_\varepsilon \sim Re_\lambda^{-1}$, which is consistent with non-equilibrium turbulence (Vassilicos 2015).

1. Introduction

Turbulence is present in the motion of fluids and plasmas, and governs many mechanisms existing in astrophysics, geophysics, biology and engineering (Davidson 2004). Because of its ability to predict many important statistical quantities characterizing turbulence, the theory of hydrodynamic turbulence formulated by Kolmogorov occupies a unique position in the study of turbulence. Indeed, in one way or another, virtually all known results can be related to well-known results from the theory of Kolmogorov. The theory is based on the Richardson-Kolmogorov energy cascade picture, whereby the turbulent kinetic energy of the flow per unit mass $u_i'u_i'/2$ (u_i' is the fluctuating velocity vector), primarily associated with the large-scale eddies, is continuously transferred into

† Email address for correspondence: watanabe.tomoaki@c.nagoya-u.jp

smaller and smaller eddies, through a non-linear inviscid process, until the kinematic viscosity ν becomes important (for small-scale eddies) and the energy is dissipated into heat (Richardson 1922). One of the key assumptions of this theory is the scale separation (Kolmogorov 1941), which is used to explain one of the most interesting features of turbulent flows: the dissipation anomaly. Indeed, it has been observed that the mean viscous dissipation rate of kinetic energy per unit mass $\langle\varepsilon\rangle = \langle\nu S_{ij}S_{ij}\rangle$ [ν: kinematic viscosity; $S_{ij} = (\partial u_i/\partial x_j + \partial u_j/\partial x_i)/2$: rate of strain tensor; $\langle\cdot\rangle$: an averaged value] is independent of viscosity in various turbulent flows at high Reynolds number. This dissipation law is mathematically expressed as the constancy of the non-dimensional dissipation rate $C_\varepsilon = \langle\varepsilon\rangle L/u_{rms}^3$ (Davidson 2004), where L is the integral scale of turbulence and u_{rms} is the root-mean-squared (rms) velocity fluctuation.

However, several experimental and numerical works (Seoud & Vassilicos 2007; Valente & Vassilicos 2012; Valente *et al.* 2014) have shown that in many flows there are important regions where the dissipation law is not observed. (Vassilicos 2015). Indeed, a power law of $C_\varepsilon \sim Re_\lambda^{-1}$ has been observed to hold in the flow behind a grid (Valente & Vassilicos 2012), which prompted researchers to revisit many classical results for canonical flows such as axisymmetric wake and planar jet (Nedić *et al.* 2013; Layek & Sunita 2018).

The non-dimensional dissipation rate and the scaling of kinetic energy dissipation rate have been also studied in canonical free shear flows, such as turbulent jets and mixing layers (Antonia *et al.* 1980; Deo *et al.* 2008, 2013; Takamure *et al.* 2019). Most of these studies discussed the streamwise evolution of these quantities on the centreline of the flow. However, one of the most important features of free shear flows is the outer intermittency, and one can find both turbulent and non-turbulent fluids at a given location in the intermittent region. The turbulent and non-turbulent fluids are separated by a thin interfacial layer: the so-called turbulent/non-turbulent interfacial (TNTI) layer. Turbulent and non-turbulent fluid regions can be distinguished by using the vorticity (Corrsin & Kistler 1955). It has been shown that the non-turbulent fluid gains vorticity by viscous diffusion near the TNTI layer (Holzner *et al.* 2008), and that vorticity diffusion causes the outward propagation of the outer edge of the turbulent region.

The kinetic energy dissipation rate near the TNTI layer is in many ways a key quantity for turbulence, since it relates to the smallest scale of motion in the flow given as the Kolmogorov scale. Indeed, various quantities characterising the TNTI layer were shown to scale with the Kolmogorov scales. The propagation velocity of the outer edge of the turbulent region was found to scale with the Kolmogorov velocity scale $v_\eta = (\nu\langle\varepsilon\rangle)^{1/4}$ (Holzner & Lüthi 2011; Wolf *et al.* 2012, 2013; Jahanbakhshi & Madnia 2016). The thickness of the TNTI layer was also shown to have 10-15 times Kolmogorov length scale $\eta = (\nu^3/\langle\varepsilon\rangle)^{1/4}$ (Watanabe *et al.* 2015; Silva *et al.* 2018). The entrained fluid motion across the entire TNTI layer is also related to the kinetic energy dissipation rate (Watanabe *et al.* 2016*b*, 2017*a*). In turbulent boundary layers, the kinetic energy dissipation rate in turbulent regions varies significantly in a wall-normal direction. Thus, in that case, it is the kinetic energy dissipation rate near the TNTI layer, which is very different from the value near the wall, that characterizes the statistics of the TNTI layer (Borrell & Jiménez 2008; Watanabe *et al.* 2018*b*; Zhang *et al.* 2018). da Silva (2009) showed the existence of a strong imbalance between interscale energy transfer and viscous dissipation near the TNTI layer. Another example where the kinetic energy dissipation rate near the TNTI layer becomes important is when modelling the scalar dissipation rate or related quantities in numerical simulations of turbulent reacting flows (Fox 2003; Mitarai *et al.* 2005; Cleary & Klimenko 2009), because the reaction zone often appears near the outer edge of the turbulent region in non-premixed jet flames (Gampert *et al.*

2014*b*). Therefore, a better understanding of behaviour of the kinetic energy dissipation rate near the TNTI layer is expected to contribute to improvements of numerical simulations of turbulent reacting flows.

Even though the kinetic energy dissipation rate near the TNTI layer is known as an important quantity, the non-dimensional dissipation rate has never been studied near the TNTI layer before. The characteristics of this layer have been studied mainly using averages conditioned on a distance from the isosurface of vorticity magnitude that marks the TNTI layer (Bisset *et al.* 2002). This method has been proved to be useful for investigating turbulent characteristics in the intermittent region, because the statistics are obtained separately for turbulent and non-turbulent fluid regions. However, the conditional averages used in existing literatures only give one-point statistics, and cannot be used for computing the integral length scale of the flow. It seems that lack of a method to compute the integral length scale of turbulence near the TNTI layer is the main reason why the non-dimensional dissipation rate has not been studied in the vicinity of the TNTI layer. A conventional approach based on auto-correlation function is not able to compute the integral length scale in the intermittent region, since this computation would involve information from both the turbulent and non-turbulent fluid regions, even though this length scale strictly concerns turbulent flow motions.

In this study, we present a new procedure which allows for the first time the computation of the integral scale of turbulence near the TNTI layer, which permits the first detailed investigation of the non-dimensional dissipation rate C_ε, within the layer. The procedure is based on volume averaging of turbulent fluids, as a function of the distance from the outer edge of the TNTI layer. The volume average is used for calculating the kinetic energy distribution, in the space of scales, near the TNTI layer, which allows the computation of the integral length scale as an energy-containing length scale. This approach is applied for direct numerical simulation (DNS) database of a planar jet, a mixing layer and a localized turbulent spot that evolves without mean shear (shear free turbulence), and we analyse the non-dimensional dissipation rate near the TNTI layer in these flows.

2. DNS of jet, mixing layer and shear free turbulence

DNS of forced homogeneous isotropic turbulence, temporally-evolving planar jet, mixing layer and shear-free turbulence were carried out to study the TNTI layer. The details of the DNS of these flows are described in da Silva & Pereira (2008); Taveira & da Silva (2014); Watanabe *et al.* (2016*a*, 2018*a*) and references therein. The governing equations of these flows are incompressible Navier–Stokes equations written as

$$\frac{\partial u_i}{\partial x_i} = 0, \tag{2.1}$$

$$\frac{\partial u_i}{\partial t} + \frac{\partial u_i u_j}{\partial x_j} = -\frac{\partial p}{\partial x_i} + \nu \frac{\partial^2 u_i}{\partial x_j \partial x_j}, \tag{2.2}$$

where u_i is the i-th component of the velocity vector, p is the pressure divided by a constant fluid density. Table 1 summarizes the main physical and computational parameters of the simulations. The size of the computational domain along the streamwise (x), cross-streamwise (y) and spanwise (z) directions (L_x, L_y, L_z) is $(6H, 10H, 4H)$ in the planar jet and $(42h_0, 54h_0, 28h_0)$ in the mixing layer, where H is the initial width of the planar jet and h_0 is the initial thickness of the mixing layer. The DNS of the planar jet and mixing layer was initialized by the mean velocity profiles given with a hyperbolic tangent function as used in previous studies (da Silva & Pereira 2008; Gampert *et al.* 2014*a*) and

Table 1: DNS of forced homogeneous isotropic turbulence, shear free turbulence, planar jet and mixing layer. ($N_x \times N_y \times N_z$) is the number of grid points.

Case	Flow	Re_0	N_x	N_y	N_z	Δ_x/η	Re_λ	δ_ν/η	δ_ω/η
HIT1	Homogeneous isotropic turbulence	943	512	512	512	1.5	172	–	–
HIT2	Homogeneous isotropic turbulence	2358	1024	1024	1024	1.4	312	–	–
SFT	Shear free turbulence	815	1024	1024	1024	1.3	180	4.3	13.2
PJET	Planar jet	10000	1200	1600	800	1.3	125	3.8	9.6
ML	Mixing layer	1000	1200	1400	800	1.1	133	3.6	10.9

velocity perturbation produced by a method based on a diffusion process (Kempf *et al.* 2005). The DNS of the planar jet and mixing layer used the code based on finite difference methods (Watanabe *et al.* 2015, 2018*a*). The DNS of shear free turbulence was started from an initial field of homogeneous isotropic turbulence and consists of a localized turbulence region displaying a turbulent front that spreads in the y direction in the absence of mean shear. Details of the shear free turbulence simulations are given in Silva *et al.* (2018). The initial isotropic turbulence field, which is subsequently used in the shear free simulations, is statistically stationary thanks to the addition of an artificial forcing described in Alvelius (1999), which is delta-correlated in time and uncorrelated with the velocity field. The power input is prescribed by a Gaussian function that affects only the smallest wave numbers $k = 2, 3$ and 4, and which is concentrated in wave number $k = 3$. Homogeneous isotropic turbulence and shear free turbulence were simulated in a periodic box with size $(2\pi)^3$ with the code based on classical pseudo-spectral methods (da Silva & Pereira 2008; Taveira & da Silva 2014). The shear free turbulence, temporal planar jet and temporal mixing layer are statistically homogeneous on a x-z plane, and the average is taken on a homogeneous plane as a function of y at each time step. The statistics in the homogeneous isotropic turbulence are computed by taking an average in the computational domain. The global Reynolds number Re_0 is defined as $u_{rms}L/\nu$ in homogeneous isotropic turbulence and shear free turbulence with rms velocity fluctuation in the x direction, u_{rms}, and integral length scale L computed with the longitudinal auto-correlation function in the x direction. For the planar jet and mixing layer, $Re_0 = U_J H/\nu$ and $U_0 h_0/\nu$ are shown in the table, respectively, where U_J is the initial centreline velocity in the jet and U_0 is the velocity difference across the mixing layer. The resolution of each simulation is assessed through Δ_x/η in table 1, where Δ_x is the grid spacing and η is the Kolmogorov length scale. $Re_\lambda = u_{rms}\lambda/\nu$ is the Reynolds number based on the Taylor microscale λ computed with the velocity component in the x direction. These statistics in the shear free turbulence, planar jet and mixing layer are computed on the centreline of the flows in the fully-developed turbulent state.

3. Statistics conditioned on the distance from the outer edge of the TNTI layer

In the shear free turbulence, planar jet and mixing layer, turbulent and non-turbulent fluid regions are bounded by a TNTI layer, which is best detected by using the vorticity (Corrsin & Kistler 1955). Following several previous works, the outer boundary separating the turbulent from the non-turbulent fluid regions is detected as the isosurface

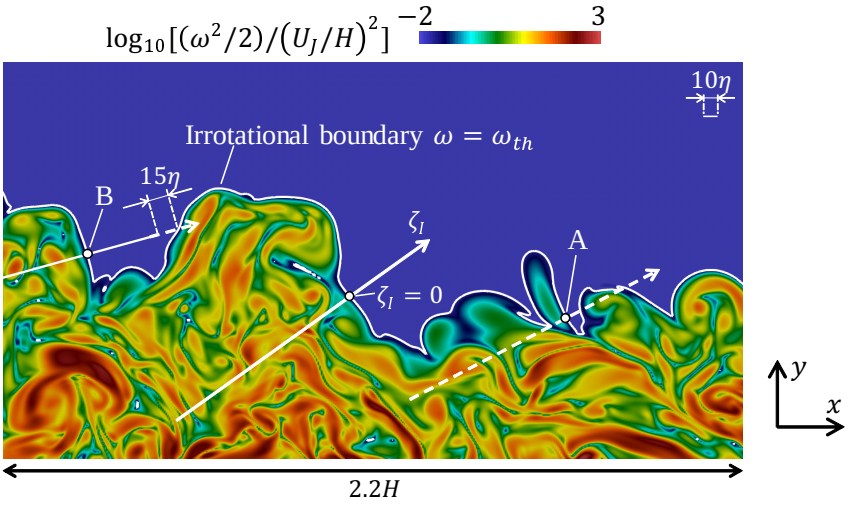

Figure 1: A colour contour of enstrophy in the intermittent region with the irrotational boundary shown with isoline of $|\boldsymbol{\omega}| = \omega_{th}$ on a x–y plane in the planar jet simulation. The broken line on the local coordinate is excluded from the conditional analysis.

of vorticity magnitude $|\boldsymbol{\omega}| = \omega_{th}$, where ω_{th} is determined by assessing how the volume of the turbulent region depends on the threshold (Taveira *et al.* 2013; Watanabe *et al.* 2014; Jahanbakhshi *et al.* 2015). Since the vorticity magnitude increases from the isosurface of $|\boldsymbol{\omega}| = \omega_{th}$ towards the inside of the turbulent region, and the isosurface is bounded by the irrotational fluid region, this isosurface of $|\boldsymbol{\omega}| = \omega_{th}$ is called the irrotational boundary (Watanabe *et al.* 2015). It is important to recall that the position of the irrotational boundary obtained with the procedure described above and in Taveira *et al.* (2013) guarantees that the irrotational boundary position is unambiguously determined as are the statistics obtained in relation to this position. This is because ω_{th} used to determine the irrotational boundary is taken from a particular wide range of values where, varying the value of ω_{th} changes the position of the irrotational boundary by a distance smaller than the Kolmogorov scale [see Silva *et al.* (2018)].

A colour contour of $\log_{10}(\omega^2/2)$ on a x–y plane in the intermittent region is shown for PJET with the isoline of $|\boldsymbol{\omega}| = \omega_{th}$ in figure 1. A local coordinate ζ_I with the origin at the irrotational boundary is taken in the normal direction of the isosurface $\mathbf{n} = -\nabla\omega^2/|\nabla\omega^2|$ as shown in the figure. Note that ζ_I is shown on a two-dimensional plane for the sake of the explanation even though ζ_I is taken in the direction of the three-dimensional vector $\mathbf{n}$. The turbulent and non-turbulent regions correspond to $\zeta_I < 0$ and $\zeta_I > 0$, respectively ($\zeta_I = 0$ at the irrotational boundary). The statistics conditioned on ζ_I are computed with the same method as in Watanabe *et al.* (2018*b*). The local coordinate ζ_I is set up for each location of $|\boldsymbol{\omega}| = \omega_{th}$, and the quantities computed on the DNS grid are interpolated onto the local coordinate with a tri-linear interpolation. Then, the conditional average on ζ_I denoted by $\langle\cdot\rangle_I$ is computed. The conditional statistics should be computed separately for turbulent and non-turbulent fluids even though sometimes, as shown in the figure, the local coordinate system crosses more than two irrotational boundary points. Here, following to Watanabe *et al.* (2018*b*), some parts of the local coordinate are excluded so that averages of turbulent and non-turbulent fluids are obtained for $\zeta_I < 0$ and $\zeta_I > 0$, respectively. When the local coordinate crosses more than two irrotational boundary points, the distance from $\zeta_I = 0$ to another irrotational boundary, Δ_ζ, is computed. In

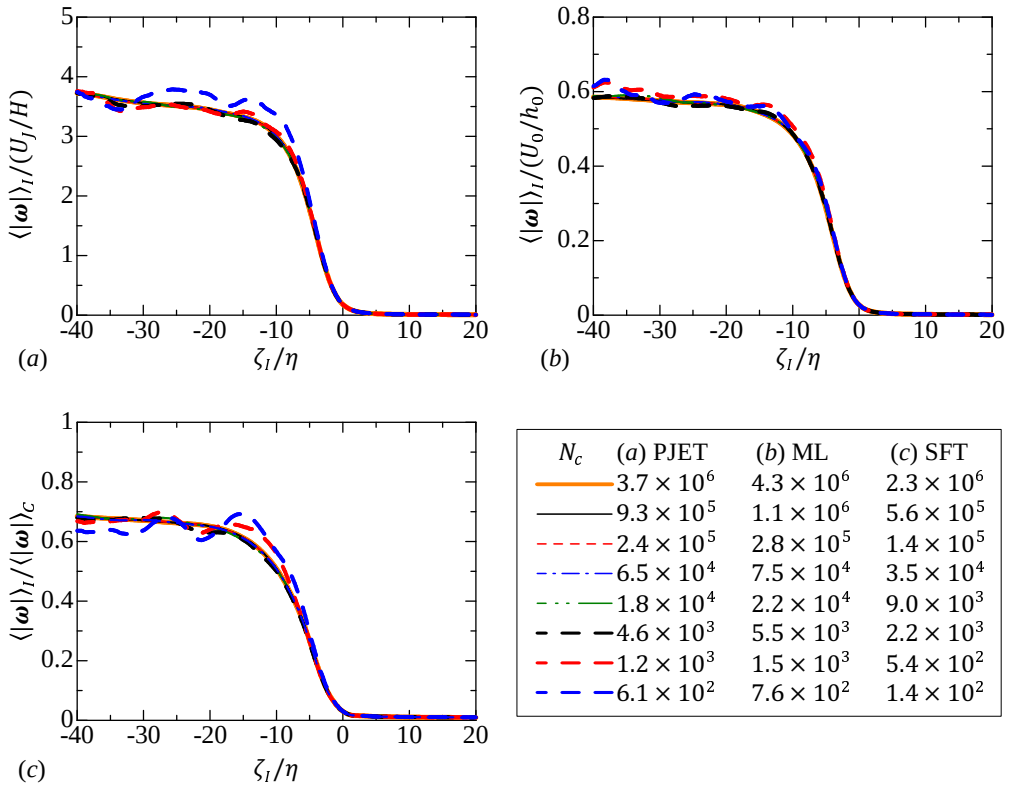

Figure 2: Influences of the number of samples on the conditional mean vorticity magnitude $\langle|\boldsymbol{\omega}|\rangle_I$ in cases (*a*) PJET, (*b*) ML and (*c*) SFT. In (*c*), $\langle|\boldsymbol{\omega}|\rangle_I$ is normalized by the mean vorticity magnitude on the centreline $\langle|\boldsymbol{\omega}|\rangle_C$.

the case that Δ_ζ is smaller than 15η (example A in figure 1), this local coordinate is not used in the conditional average. For $\Delta_\zeta > 15\eta$, samples for conditional statistics are not taken from the region within a distance of 15η from another irrotational boundary (example B in figure 1). Here, η is taken on the centreline of the flows, and 15η is chosen based on the mean thickness of the TNTI layer (Silva *et al.* 2018). The particular choice of 15η does not affect the resulting conditional statistics, and it was confirmed that the conditional statistics do not change in the range of 5η-25η (Watanabe *et al.* 2018*b*).

The number of samples used in the conditional profiles increases with the number of the points, N_c, on the isosurface of $|\boldsymbol{\omega}| = \omega_{th}$ used for setting the local coordinate, from which the samples are taken. Figure 2 compares the conditional mean vorticity magnitude $\langle|\boldsymbol{\omega}|\rangle_I$ obtained for a wide range of N_c, where ζ_I is normalized by the Kolmogorov scale η on the centreline. $\langle|\boldsymbol{\omega}|\rangle_I$ decreases across the TNTI layer from the turbulent toward non-turbulent region. As N_c increases, the curve tends to collapse onto a single curve. The scatter due to a small number of samples is prominent for $N_c < 10^4$, while $\langle|\boldsymbol{\omega}|\rangle_I$ becomes independent of N_c for $N_c > 10^4$. In the present study, the conditional statistics are computed with $N_c = 3.5\times10^4$, 6.5×10^4 and 7.5×10^4 in cases SFT, PJET and ML.

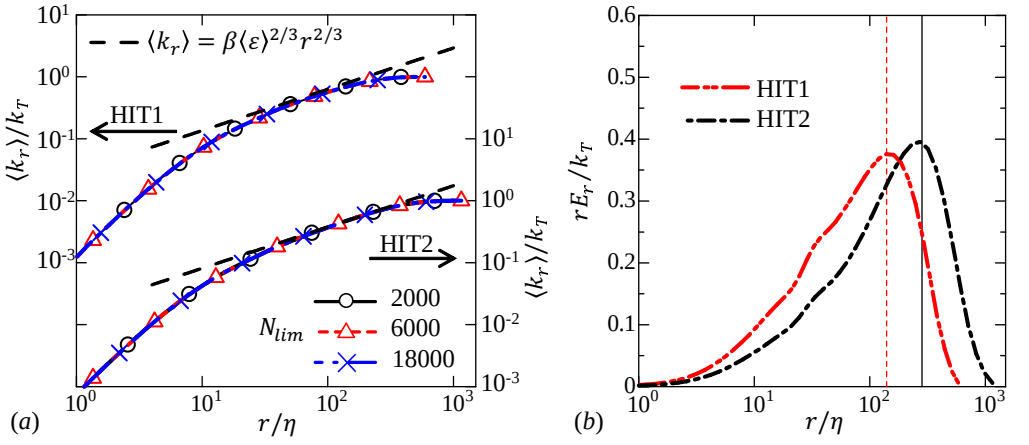

Figure 3: (a) Cumulative kinetic energy $\langle k_r\rangle$ normalized by the turbulent kinetic energy k_T in cases HIT1 and HIT2 for several values of N_{lim}. The theoretical curves $\beta\langle\varepsilon\rangle^{2/3}r^{2/3}$ (with $\beta = 2$) are also shown. (b) Contribution to the kinetic energy from scale r, rE_r, normalized by the turbulent kinetic energy k_T.

4. Scale decomposition near the turbulent/non-turbulent interface

4.1. *Local spherical volume averages*

In order to compute the turbulent characteristics near the TNTI layer, we use local volume averages in a sphere, denoted by an overbar, where for each sphere of radius r centred at point $\mathbf{x}$, a spherical volume average of a variable $\phi(\mathbf{x})$ is defined by (Watanabe & Nagata 2016),

$$\overline{\phi}(\mathbf{x},r) = \frac{\iiint G(\mathbf{x},\mathbf{x}',r)\phi(\mathbf{x}')d\mathbf{x}'}{V_R} = \frac{1}{N_p}\sum_{n=1}^{N_p}\phi[\mathbf{x}^{(n)}],$$

where $V_R(r)$ is the volume of the sphere and $G(\mathbf{x})$ is a kernel function which is equal to 1 and 0 inside and outside the sphere, respectively. This average corresponds to a low-pass filter operation with a cut-off length proportional to r (Pumir *et al.* 2001), whereby $\phi(\mathbf{x})$ can be decomposed into large-scale ($\overline{\phi}$) and small-scale components (ϕ''), *i.e.* $\phi(\mathbf{x}) = \overline{\phi}(\mathbf{x},r) + \phi''(\mathbf{x},r)$. Here, a single length scale r is used without distinguishing orientations.

In practice, the computation is carried out by taking N_p fluid points randomly placed within the sphere, and by interpolating the value of the fluid variable $\phi(\mathbf{x})$ on each point $\mathbf{x}^{(n)}$ using a tri-linear interpolation, as indicated in the last term of the equation above. The number of points N_p, used for each sphere of radius r, is set as $N_p = \min[(r/20\eta)^3, N_{lim}]$, where the parameter N_{lim} is chosen to limit the computational cost while $(r/20\eta)^3$ ensures that the computational method used here is equivalent to the definition of the local volume average. When $(r/20\eta)^3$ is smaller than 20, $N_p = 20$ is used instead of $(r/20\eta)^3$. Additionally, an ensemble average of spheres, $\langle\overline{\phi}\rangle(r)$, can be taken by using a large number of equally sized spheres located at different points $\mathbf{x}$ within the computational domain.

We start by showing that using the new spherical volume average metric, one recovers the classical results observed in homogeneous isotropic turbulence. Specifically, we consider the kinetic energy averaged in a sphere, $k(\mathbf{x},r) = \overline{u_i(\mathbf{x})u_i(\mathbf{x})}/2$, split into two

contributions resulting from the spherical average: $k(\mathbf{x},r) = k_m(\mathbf{x},r) + k_r(\mathbf{x},r)$, where $k_m(\mathbf{x},r) = \overline{u}_i\overline{u}_i/2$ involves the contribution from the sphere's centre-of-mass (mean) motion, whereas $k_r(\mathbf{x},r) = \overline{u_i''u_i''}/2$ represents the contribution from (relative) motion in relation to the sphere's centre-of-mass. From these definitions, one can interpret the ensemble average of $k_r(\mathbf{x},r)$ as the cumulative kinetic energy held in scales smaller than r, such that $\langle k_r\rangle$ for large r is equal to the turbulent kinetic energy $k_T = \langle u_i'u_i'\rangle/2$. The brackets $\langle\ \rangle$ represent a spatial average. For computing $\langle k_r\rangle$ in homogeneous isotropic turbulence, the spatial average used a large number of spheres (centred at different locations in the computational domain). Furthermore, a kinetic energy density at scale r can be defined by $E_r = \partial\langle k_r\rangle/\partial r$, whose integral gives the total kinetic energy as $k_T = \int_0^\infty E_r dr$ (Townsend 1976).

Figure 3(a) shows $\langle k_r\rangle$ in homogeneous isotropic turbulence (cases HIT1 and HIT2) for three different values of N_{lim}. $\langle k_r\rangle$ increases with the radius of the sphere r as expected from the definition, and for an intermediate range of r, it closely follows the inertial range law $\langle k_r\rangle = \beta\langle\varepsilon\rangle^{2/3}r^{2/3}$ (with $\beta = 2$) predicted by Kolmogorov for the second-order velocity structure function (Davidson 2004), which is also a measure of the cumulative kinetic energy (Townsend 1976). Here, the broken line that represents $\langle k_r\rangle = \beta\langle\varepsilon\rangle^{2/3}r^{2/3}$ is obtained with $\langle\varepsilon\rangle$ computed from the DNS results. The scale range with $\langle k_r\rangle = \beta\langle\varepsilon\rangle^{2/3}r^{2/3}$ is wider for HIT2, which has a higher Reynolds number than HIT1. It is clear that $\langle k_r\rangle$ is quite insensitive to the value of N_{lim} provided that this number is sufficiently high, and a value of $N_{lim} = 6000$ is therefore used for the rest of the paper.

Figure 3(b) shows rE_r in semi-log coordinates, which represents the contribution to the turbulent kinetic energy from scale r. It is expected that rE_r peaks at the scale $r = L$ (Davidson 2004), where L is the integral scale defined as $L = \int_0^\infty f(r)dr$, where $f(r) = \langle u'(x)u'(x+r)\rangle/\langle u'^2(x)\rangle$ is the longitudinal auto-correlation function. In the present simulations, rE_r attains their maxima at $r = 140\eta$ and $r = 270\eta$, for cases HIT1 and HIT2, respectively, which compare well with $L = 140\eta$ and $L = 265\eta$ (represented by the vertical lines in figure 3(b)) directly obtained by integrating $f(r)$ for cases HIT1 and HIT2, respectively. Thus, we confirm using the present DNS that the integral scale can be obtained as the scale $r = L$ where rE_r attains its maximum.

4.2. *Conditional spherical volume averages*

The local spherical volume averages are computed near the TNTI layer in relation to the position of the irrotational boundary. A volume average of "turbulent fluids" on the local coordinate is defined by extending the spherical volume average as,

$$\overline{\phi}(\zeta_I, r) = \frac{\iiint I(\mathbf{x}')G(\zeta_I, \mathbf{x}', r)\phi(\mathbf{x}')d\mathbf{x}'}{\iiint I(\mathbf{x}')G(\zeta_I, \mathbf{x}', r)d\mathbf{x}'}, \tag{4.1}$$

where $I(\mathbf{x})$ is equal to 1 and 0 when the coordinate $\mathbf{x}$ is taken from the turbulent and non-turbulent regions, respectively. Introducing ζ_I and $I(\mathbf{x})$ allows us to investigate the statistical properties of turbulence separately from non-turbulent fluids. An ensemble average is calculated with a large number of spheres (with radius r) whose centre is located at a fixed distance ζ_I from the irrotational boundary positions, where this average is denoted by $\langle\ \rangle_{RI}$. The cumulative kinetic energy held below scale r at a distance of ζ_I from the irrotational boundary is denoted by $\langle k_r\rangle_{RI}(\zeta_I, r)$. The advantage of the present metric is that it allows one to simultaneously assess the turbulent statistics as function of the scale r and of the position ζ_I in relation to the TNTI. A classic low pass filtering operation could also be used to perform a scale separation, however the filtering procedure would include flow points from both the turbulent and non-turbulent regions.

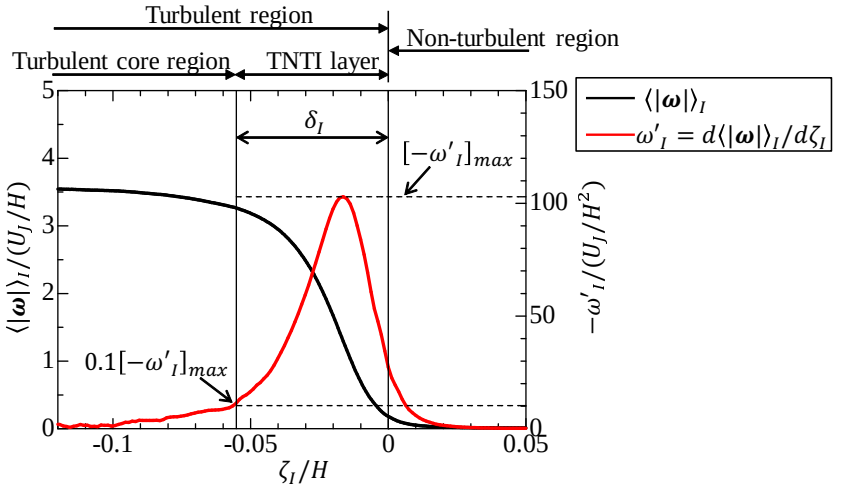

Figure 4: Conditional mean vorticity magnitude $\langle\omega\rangle_I$ and its derivative with respective to ζ_I, $\omega'_I = d\langle\omega\rangle_I/d\zeta_I$ in PJET. The thickness of the TNTI layer is denoted by δ_I.

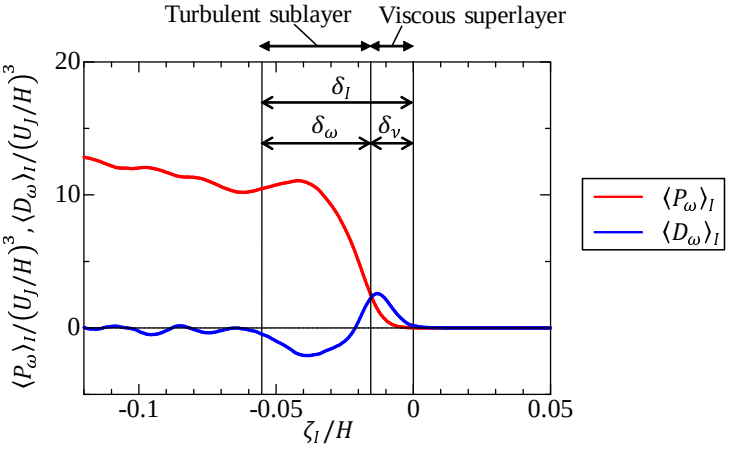

Figure 5: Conditional averages of enstrophy production term $\langle P_\omega\rangle_I$ and diffusion term $\langle D_\omega\rangle_I$ in PJET. The thicknesses of the turbulent sublayer and viscous superlayer are denoted by δ_ω and δ_ν, respectively.

We are interested in analysing the turbulent fluid near or within the TNTI layer while a sphere of radius r at some locations $\mathbf{x}$ may intersect the irrotational boundary at several points. Therefore, the non-turbulent fluid is removed from these spherical averages. Thus, we can focus on the turbulent characteristics of the turbulent fluid near the irrotational boundary.

5. Results and Discussion

5.1. *Conditional statistics near the TNTI layer*

Figure 4 shows the conditional average of vorticity magnitude $\langle|\boldsymbol{\omega}|\rangle_I$ and its derivative $\omega'_I = d\langle|\boldsymbol{\omega}|\rangle_I/d\zeta_I$ with a negative sign in PJET. $\langle|\boldsymbol{\omega}|\rangle_I$ rapidly increases from the non-

turbulent region ($\zeta_I > 0$) toward the turbulent region ($\zeta_I < 0$), and a peak of $-\omega_I'$ appears at $\zeta_I = -0.016H$. The TNTI layer can be defined as the region across which the vorticity magnitude rapidly increases from the non-turbulent region toward the turbulent region. Following to previous study (Nagata *et al.* 2018), the mean extent of the TNTI layer on the local coordinate can be quantified based on ω_I'. Here, the outer edge of the TNTI layer is located at $\zeta_I = 0$ for the present choice of the threshold. The inner edge of the TNTI layer can be identified as the location at which $-\omega_I'$ is equal to 10 % of the maximum value of $-\omega_I'$, $[-\omega_I']_{max}$. The length between the outer and inner edges of the TNTI layer yields the thickness of the TNTI layer, δ_I, as shown in figure 4, where $\delta_I = 0.055H$ is obtained. This method for estimating the TNTI layer thickness δ_I was compared with another method based on fitting an error function to conditional statistics in Watanabe *et al.* (2018*a*), where both methods were shown to give a similar value of δ_I.

The inner structures of the TNTI layer, called viscous superlayer and turbulent sublayer, are often discussed with respective to vorticity dynamics (van Reeuwijk & Holzner 2014; da Silva *et al.* 2014; Jahanbakhshi & Madnia 2018; Silva *et al.* 2018). These inner layers can be detected by analysing the enstrophy transport equation

$$\frac{D\omega^2/2}{Dt} = \omega_i S_{ij}\omega_j + \nu\nabla^2(\omega^2/2) - \nu\nabla\omega_i \cdot \nabla\omega_i = P_\omega + D_\omega + \varepsilon_\omega, \tag{5.1}$$

where $P_\omega = \omega_i S_{ij}\omega_j$ is the production term, $D_\omega = \nu\nabla^2(\omega^2/2)$ is the viscous diffusion term and $\varepsilon_\omega = -\nu\nabla\omega_i \cdot \nabla\omega_i$ is the viscous dissipation term. When non-turbulent fluids are entrained into the TNTI layer, $\omega^2/2$ increases on the entrained fluid path through P_ω and D_ω. The conditional averages of P_ω and D_ω are shown for PJET in figure 5. Note that the conditional averages of $|\boldsymbol{\omega}|$, P_ω and D_ω in a mixing layer and shear free turbulence are also similar to those in the planar jet (Watanabe *et al.* 2015, 2017*c*). Near the irrotational boundary ($\zeta_I \approx 0$), there is a region with $\langle P_\omega\rangle_I \leqslant \langle D_\omega\rangle_I$, where the enstrophy growth is dominated by the viscous diffusion. This region is called the viscous superlayer (Taveira & da Silva 2014). On the other hand, $\langle P_\omega\rangle_I$ exceeds $\langle D_\omega\rangle_I$ in the inner part of the TNTI layer, which is called turbulent sublayer (Silva *et al.* 2018). The mean thickness of the viscous superlayer δ_ν can be obtained as the distance from $\zeta_I = 0$ to the location of $\langle P_\omega\rangle_I = \langle D_\omega\rangle_I$. Then, the mean thickness of the turbulent sublayer, δ_ω, can be obtained as $\delta_\omega = \delta_I - \delta_\nu$. Values of δ_ω and δ_ν divided by Kolmogorov scale η on the centreline ($y = 0$) are shown in table 1. Similar values of δ_ω/η and δ_ν/η were also reported in various flows (Silva *et al.* 2018; Zhang *et al.* 2018; Nagata *et al.* 2018), and agree with the scaling of the TNTI layer at high Reynolds numbers and of its sublayers, recently analysed in Silva *et al.* (2018).

Based on δ_I, δ_ω and δ_ν obtained in this way, the TNTI layer, viscous superlayer and turbulent sublayer, can be identified in the plots of conditional statistics as shown in figures 4 and 5. Furthermore, the turbulent region for $\zeta_I \leqslant -\delta_I$ is called a turbulent core region in figure 5. Then, the local coordinate ζ_I is divided into four regions: non-turbulent region, viscous superlayer, turbulent sublayer and turbulent core region. Identifying these regions is useful to interpret various statistics obtained near the TNTI layer. For example, the boundary between the viscous superlayer and turbulent sublayer was shown to have a large scalar dissipation rate and its production rate (Watanabe *et al.* 2015). The movement of entrained fluid particles with respective to the irrotational boundary location was also shown to have different scalings between the turbulent sublayer and viscous superlayer (Watanabe *et al.* 2016*b*). The turbulent sublayer also exhibits different statistical properties from the turbulent core region [e.g. alignment between vorticity vector and eigenvectors of strain-tensor (Watanabe *et al.* 2014)]. For this reason, the

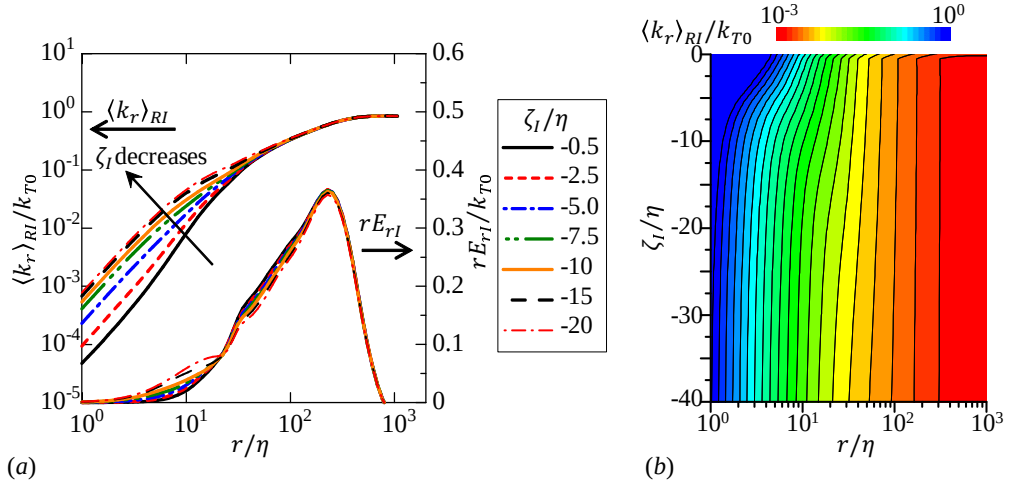

Figure 6: Conditional average of relative kinetic energy $\langle k_r \rangle_{RI}$ as a function of the distance ζ_I from the irrotational boundary and the size of the sphere r for shear free turbulence: (a) dependence on r for several distances from the irrotational boundary, $-20 \leqslant \zeta_I/\eta \leqslant -0.5$ (the conditional energy density rE_{rI} is also shown); (b) contours of $\langle k_r \rangle_{RI}$ on (ζ_I, r) for $-20 \leqslant \zeta_I/\eta \leqslant -0.5$, and $10^0 \leqslant r/\eta \leqslant 10^3$. $\langle k_r \rangle_{RI}$ is normalized by the turbulent kinetic energy on the centreline of turbulence, k_{T0}.

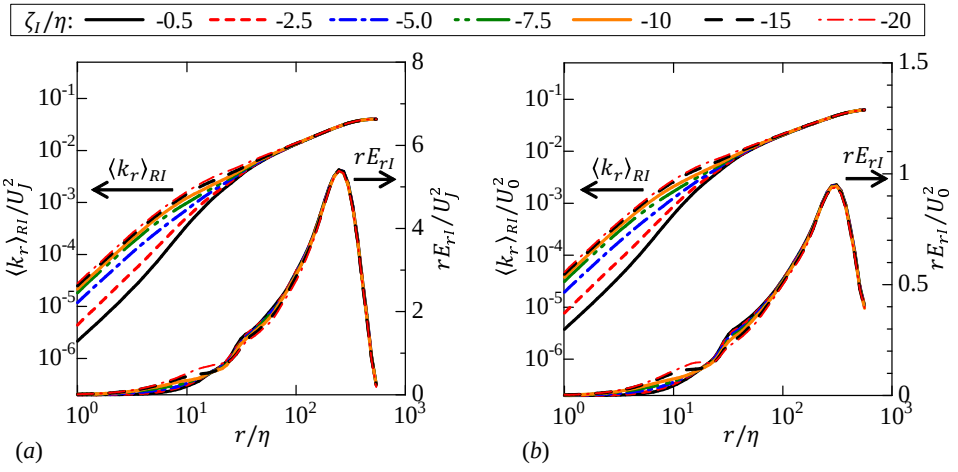

Figure 7: Conditional average of relative kinetic energy $\langle k_r \rangle_{RI}$ and conditional energy density rE_{rI} in cases (a) PJET and (b) ML.

conditional statistics are presented with marks that represent the boundaries between these four regions. It should be noted that the viscous terms are not dominant in the kinetic energy budget within the viscous superlayer. Pressure diffusion of kinetic energy also has an important contribution in the kinetic energy budget within the TNTI layer (Taveira & da Silva 2013; Terashima *et al.* 2016; Watanabe *et al.* 2016*a*).

5.2. *Conditional statistics with volume average near the TNTI layer*

The conditional statistics are computed with the volume average (4.1) in the shear free turbulence, planar jet and mixing layer. Figure 6(a) plots the cumulative kinetic energy $\langle k_r \rangle_{RI}$ against r/η obtained at different locations on ζ_I in shear free turbulence while figure 6(b) shows a colour contour of $\langle k_r \rangle_{RI}$ as a function of $(r/\eta, \zeta_I/\eta)$. For $\zeta_I/\eta > -10$, $\langle k_r \rangle_{RI}$ for small r notably decreases with ζ_I, which indicates a depletion of kinetic energy at small scales within the TNTI layer. da Silva & Pereira (2008) showed that the irrotational motions outside the irrotational boundary are dominated by the large scales. However, the cumulative kinetic energy further shows that the energy distribution across scales begins to change within the TNTI layer. As in homogeneous isotropic turbulence, the integral scale of turbulence near the TNTI layer is estimated using the kinetic energy density $E_{rI} = \partial \langle k_r \rangle_{RI} / \partial r$ premultiplied by r as shown in figure 6(a). The peak location of rE_r that yields the integral length scale near the TNTI layer, L_I, is insensitive to ζ_I in agreement with the rapid distortion theory applied for the TNTI layer (Teixeira & da Silva 2012).

Figure 7 shows the cumulative kinetic energy $\langle k_r \rangle_{RI}$ and kinetic energy density rE_r near the TNTI layer for cases PJET and ML. Here, the range of r is chosen to present the results for the length scales from the Kolmogorov scale $r/\eta = 1$ to the length scale of the peak in rE_r. The dependence of $\langle k_r \rangle_{RI}$ and rE_r on r and ζ_I is similar for all flows. The cumulative kinetic energy $\langle k_r \rangle_{RI}$ in small scales decreases as ζ_I becomes close to 0, and small-scale motions are less active as the irrotational boundary $\zeta_I = 0$ is approached from the turbulent region. The scale at which rE_r peaks hardly depends on ζ_I in the planar jet and mixing layer. The integral length scale L_I at each ζ_I can be obtained as the length r at which rE_r peaks, where rE_r is computed for a wide range of r and ζ_I. However, L_I does not change with ζ_I as confirmed from the peak in rE_r in figures 6(a) and 7. The values of L_I in the shear free turbulence, planar jet and mixing layer are $L_I = 1.9L_0$, $L_I = 1.0H = 2.0L_0$ and $L_I = 9.9h_0 = 2.3L_0$, respectively, where L_0 is the integral length scale at $y = 0$, obtained by integrating the longitudinal autocorrelation function of the velocity fluctuation in the x direction.

5.3. *Non-dimensional dissipation rate near the TNTI layer*

The non-dimensional dissipation rate in free shear flows has been studied on the centreline of the flow, where it is calculated with the averaged energy dissipation rate and turbulent kinetic energy (or root-mean-squared streamwise velocity fluctuation) defined as one-point statistics and with the integral length scale computed with an auto-correlation function (Antonia *et al.* 1980; Deo *et al.* 2008, 2013; Takamure *et al.* 2019). Similarly, the non-dimensional dissipation rate near the TNTI layer is calculated with the averaged kinetic energy dissipation rate $\langle \varepsilon \rangle_I$, turbulent kinetic energy $k_{TI} = (\langle u_j u_j \rangle_I - \langle u_j \rangle_I \langle u_j \rangle_I)/2$ and the integral length scale L_I, where $\langle \varepsilon \rangle_I$ and k_{TI} are obtained as one-point statistics on the local coordinate. Figures 8(a-c) show $\langle \varepsilon \rangle_I$, k_{TI} and the turbulent Reynolds number $Re_\lambda = (2k_{TI}/3)^{1/2} \lambda_I / \nu$ near the TNTI layer in the shear free turbulence, mixing layer and planar jet, where $\lambda_I = (10\nu k_{TI}/\langle \varepsilon \rangle_I)^{1/2}$ is the Taylor microscale. Note that the volume average (4.1) is not used for these quantities, and the conditional averages are simply taken on the local coordinate. Both $\langle \varepsilon \rangle_I$ and k_{TI} decrease when approaching the irrotational boundary from the turbulent region. However, Re_λ sharply increases in the viscous superlayer region and in the non-turbulent region, in agreement with Teixeira & da Silva (2012).

The results from figures 8(a-c), 6(a) and 7 allow us to observe for the first time the non-dimensional energy dissipation rate C_ε near the TNTI layer. Figure 8(d) shows the

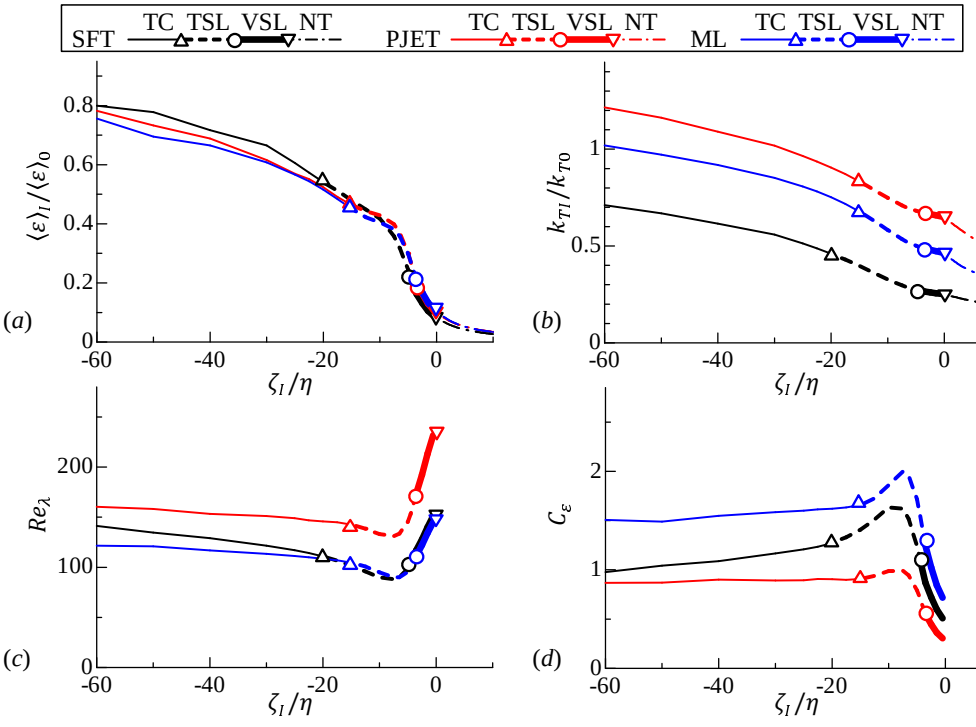

Figure 8: Conditional statistics in relation to the irrotational boundary: (a) averaged viscous dissipation rate ε; (b) turbulent kinetic energy k_{TI}; (c) turbulent Reynolds number Re_λ; (d) non-dimensional dissipation rate C_ε. Different lines highlight the two sublayers that exist within the TNTI layer between the turbulent core (TC) and the non-turbulent region (NT): the viscous superlayer (VSL) and turbulent sublayer (TSL). Subscript 0 denotes the value taken at the centre of turbulence.

profile of C_ε, which is computed directly from its definition as $\langle\varepsilon\rangle_I L_I/(2k_{TI}/3)^{3/2}$. Here, C_ε is shown for the turbulent region since the integral length scale is obtained as a length scale of turbulence. In the turbulent core region, C_ε is roughly constant in the three flows with $1.0 \lesssim \langle C_\varepsilon\rangle_I \lesssim 1.5$, which is close to the value of $C_\varepsilon \approx 1.0$ observed for decaying isotropic turbulence (Sreenivasan 1984). However, C_ε exhibits a peculiar evolution near the TNTI in all the flows studied here, raising into a peak roughly at the middle of the turbulent sublayer at $\zeta_I/\eta \approx -10$, before sharply decreasing inside the viscous superlayer.

The spatial variation of C_ε is investigated in relation to the turbulent Reynolds number within the TNTI layer. Figure 9(a) plots C_ε against Re_λ in the turbulent sublayer and viscous superlayer. As Re_λ decreases from the viscous superlayer toward the turbulent sublayer, C_ε increases, where a power law $C_\varepsilon \sim Re_\lambda^{-2}$ is clearly found for all flows. Figure 9(b) plots C_ε premultiplied by Re_λ^2 against Re_λ for confirming the relation $C_\varepsilon \sim Re_\lambda^{-2}$, which appears as a horizontal line, and shows that the relation $C_\varepsilon \sim Re_\lambda^{-2}$ holds from the viscous superlayer to the middle of the turbulent sublayer. Clearly the relation $C_\varepsilon \sim Re_\lambda^{-2}$ arises mainly from the viscous superlayer, where viscous effects dominate enstrophy. The fact that the same relation is observed in part of the turbulent sublayer is not easy to explain. The concepts of the viscous superlayer and turbulent sublayer are defined in relation to the enstrophy, which is a small-scale quantity, unlike the velocity, which impacts in the definition of C_ε. Clearly, from its definition, the viscous superlayer is

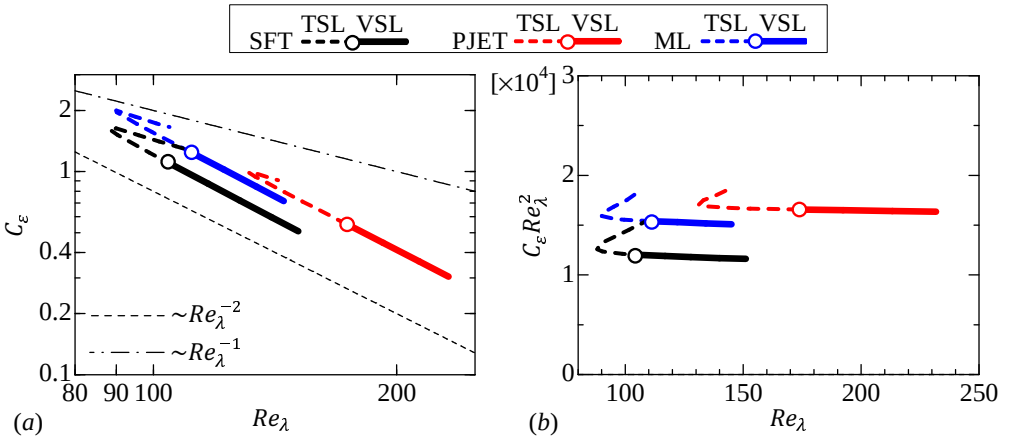

Figure 9: Normalized energy dissipation rate C_ε as a function of the turbulent Reynolds number Re_λ in the viscous superlayer and turbulent sublayer: (a) a logarithmic plot of $(C_\varepsilon, Re_\lambda)$; (b) a linear plot of $(C_\varepsilon Re_\lambda^2, Re_\lambda)$. Different lines are used for the turbulent sublayer (TSL) and viscous superlayer (VSL).

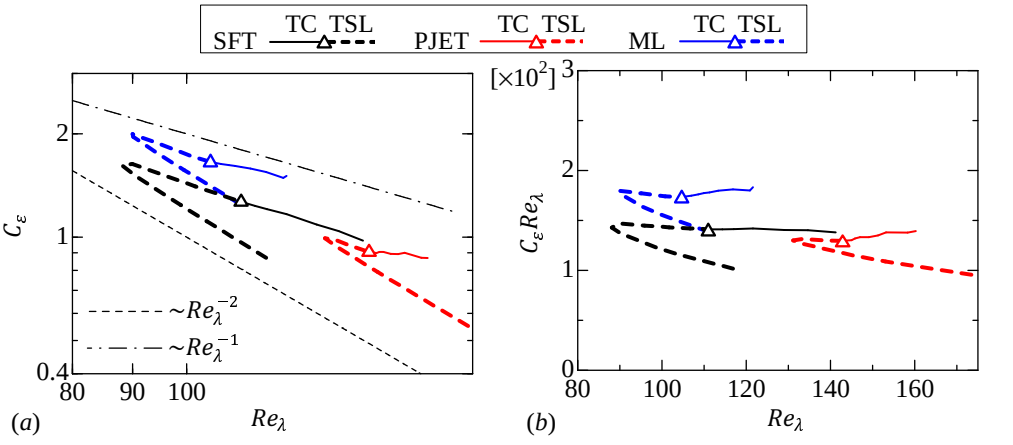

Figure 10: Normalized energy dissipation rate C_ε as a function of the turbulent Reynolds number Re_λ in the turbulent sublayer and turbulent core region: (a) a logarithmic plot of $(C_\varepsilon, Re_\lambda)$; (b) a linear plot of $(C_\varepsilon Re_\lambda, Re_\lambda)$. Different lines are used for the turbulent core (TC) and turbulent sublayer (TSL).

dominated by enstrophy viscous diffusion. On the other hand, enstrophy production is dominant in the enstrophy growth in the turbulent sublayer. However, in practice there is of course a small overlap between the two effects - viscous diffusion and production - at the boundary between the viscous superlayer and turbulent sublayer, *i.e.* viscous effects do not end abruptly when we move from the viscous superlayer into the turbulent sublayer. To complicate the matters, C_ε depends not only on the small scales, which are related to the definition of the viscous superlayer and turbulent sublayer, but also on the velocity fluctuations associated with the large scales of motion with no direct link to the

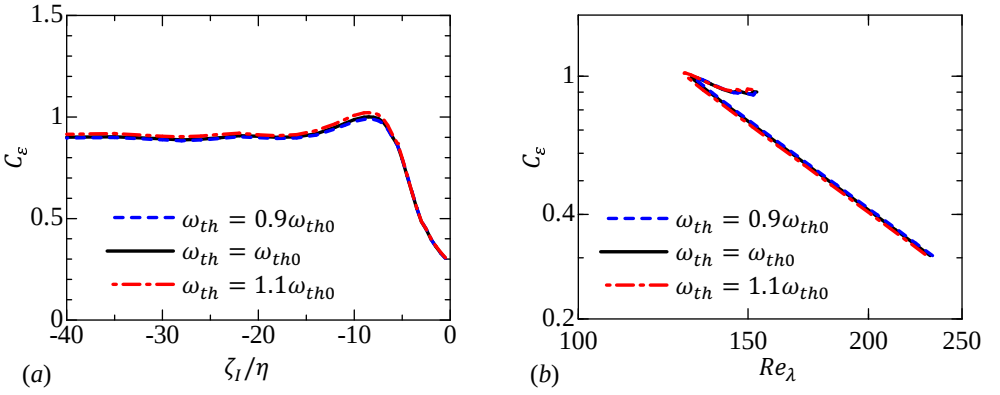

Figure 11: Influences of the threshold ω_{th} used for detecting the irrotational boundary in PJET. C_ε plotted against (*a*) ζ_I/η and (*b*) Re_λ for $\omega_{th} = 0.9\omega_{th0}$, ω_{th0} and $1.1\omega_{th0}$, where $\omega_{th0} = 0.18(U_J/H)$ is used in the present analysis.

definition of the two sub-layers. The origin of $C_\varepsilon \sim Re_\lambda^{-2}$ is discussed further below and in the Appendix.

Figure 10(*a*) plots C_ε against Re_λ in the turbulent sublayer and turbulent core region. At the local minimum of Re_λ found in the turbulent sublayer [in figure 8(*c*)], the relation between C_ε and Re_λ is changed, and $C_\varepsilon \sim Re_\lambda^{-1}$ follows in the rest of the turbulent sublayer. Figure 10(*b*) plots $C_\varepsilon Re_\lambda$ against Re_λ for confirming the relation $C_\varepsilon \sim Re_\lambda^{-1}$, and thus $C_\varepsilon Re_\lambda$ tends to be constant in the turbulent sublayer and turbulent core region. The relation $C_\varepsilon \sim Re_\lambda^{-1}$ was also observed in non-equilibrium turbulence (Vassilicos 2015).

In previous studies of non-equilibrium turbulence, the scaling $C_\varepsilon \sim Re_\lambda^{-1}$ has been explained as influences of the large-scale coherent structures (Goto & Vassilicos 2016) or as a non-equilibrium perturbation correction to the Kolmogorov equilibrium spectrum (Bos & Rubinstein 2017). In the analysis of the TNTI layer, the relation $C_\varepsilon \sim Re_\lambda^{-1}$ is observed here for three very different flows, which have different large-scale structures and it is unclear how spectral spikes described in Goto & Vassilicos (2016) could explain this scaling. Recall that in the shear free turbulence case, the typical large-scale eddies are somehow different from the ones observed in other flows, such as free shear flows. It is noteworthy that the energy spectra of streamwise velocity fluctuations in the temporally-evolving mixing layer and planar jet, observed in previous studies, did not show any clear spikes at the large scales (Watanabe *et al.* 2017*b*; Watanabe & Nagata 2017), but we cannot completely rule out the possibile influences of these spikes that might exist in early times of the simulations. On the other hand, the analysis considered in Bos & Rubinstein (2017) is for relatively small perturbations, whereas the perturbations found within the turbulent sublayer are not likely small, since there are many possible reasons that can induce perturbations in the vicinity of the TNTI layer. For example, it was shown that the kinetic energy near the TNTI layer is transferred in physical space by pressure diffusion, whose contribution depends on the associated length scales (Taveira & da Silva 2013; Terashima *et al.* 2016; Watanabe *et al.* 2016*a*). As suggested by an anonymous referee it is also possible that none of these explanations can be used to describe the observed relation $C_\varepsilon \sim Re_\lambda^{-1}$. What is clear at the moment is that this scaling law is robust and is consistently observed in the turbulent sublayer of very different flow configurations.

Figure 6 shows that the integral length scale L_I is almost constant near the TNTI

layer. In figures 8(a) and (b), although both averaged energy dissipation rate $\langle\varepsilon\rangle_I$ and turbulent kinetic energy k_{TI} decrease in the turbulent region toward $\zeta_I = 0$, k_{TI} only weakly depends on ζ_I within the viscous superlayer. Assumption of constant L_I and k_{TI} yields $C_\varepsilon \sim Re_\lambda^{-2}$ from the definitions of C_ε and Re_λ, where $C_\varepsilon = \langle\varepsilon\rangle_I L_I/(2k_{TI}/3)^{3/2}$ and $Re_\lambda = (20/3\nu)^{1/2} k_{TI} \langle\varepsilon\rangle_I^{-1/2}$ can be combined to give $C_\varepsilon Re_\lambda^2 = CL_I\sqrt{k_{TI}}/\nu$ with constant C. Therefore, the power law $C_\varepsilon \sim Re_\lambda^{-2}$ observed in the viscous superlayer and turbulent sublayer is related to the faster decay of $\langle\varepsilon\rangle_I$ with ζ_I, than those of L_I and k_{TI}, as discussed in the Appendix.

Finally, figure 11 shows C_ε plotted with ζ_I/η and Re_λ obtained for different thresholds ω_{th} for PJET. Here, the results are compared among $\omega_{th} = 0.9\omega_{th0}$, ω_{th0} and $1.1\omega_{th0}$, where $\omega_{th0} = 0.18(U_J/H)$ is used in other figures. The threshold dependence is very small and we observe the same tendency in all these plots.

6. Conclusions

Direct numerical simulations of planar jet, mixing layer and shear free turbulence were used to study the non-dimensional dissipation rate C_ε, near the TNTI layer, where the turbulent Reynolds number Re_λ ranges between 120 and 180 at the centreline of the turbulent region of these flows. The analysis was made possible through the development of a new procedure based on a volume average within a sphere with radius r, which allows a detailed investigation of the scale dependence of kinetic energy near the TNTI layer. For instance, the kinetic energy density at the scale r can be computed by taking the derivative of the cumulative kinetic energy with respective to r.

To validate this method based on the volume average, several well-known turbulent statistics were first recovered in homogeneous isotropic turbulence. The cumulative kinetic energy computed with the volume averaging procedure in homogeneous isotropic turbulence was shown to increase with $r^{2/3}$ for an intermediate range of scales r, as expected from the scaling of the second-order velocity structure function. It was shown that the scale dependence of the kinetic energy density yields the integral length scale close to that obtained from auto-correlation function of velocity fluctuation.

The tools based on the volume average were combined with the conditional averages, as a function of the position within the TNTI layer ζ_I. Here, the statistics were computed only for turbulent fluid regions, by eliminating non-turbulent fluids from the volume average. For all the flows studied in the present work the kinetic energy at small scales becomes smaller as the irrotational boundary is approached (from the turbulent region). An important result was the realisation that the turbulent integral length scale L_I, estimated from the scale dependence of kinetic energy density, was shown to be almost independent of the position ζ_I near the TNTI layer. The present method uses a single length scale r without distinguishing orientations, and anisotropy of the integral length scale cannot be studied with this method.

The non-dimensional energy dissipation rate near the TNTI layer was computed as $C_\varepsilon = \langle\varepsilon\rangle_I L_I/(2k_{TI}/3)^{3/2}$ with the averaged viscous dissipation rate $\langle\varepsilon\rangle_I$ and the turbulent kinetic energy k_{TI} defined with the averages conditioned on ζ_I. The results show that for all the flows considered in this work, as the irrotational boundary is approached from the turbulent region, C_ε slightly increases and reaches its peak within the turbulent sublayer, and later decreases within the viscous superlayer. C_ε plotted against the turbulent Reynolds number Re_λ showed that C_ε within the TNTI layer exhibits two relations: $C_\varepsilon \sim Re_\lambda^{-1}$ and $C_\varepsilon \sim Re_\lambda^{-2}$. Specifically, whereas in the viscous superlayer and part of the turbulent sublayer display $C_\varepsilon \sim Re_\lambda^{-2}$, the remaining of the

turbulent sublayer exhibits $C_\varepsilon \sim Re_\lambda^{-1}$. The relation $C_\varepsilon \sim Re_\lambda^{-1}$ is consistent with the dissipation scaling observed in non-equilibrium turbulence (Vassilicos 2015).

This work was supported by JSPS KAKENHI Grant Numbers 18K13682 and 18H01367 and by "Collaborative Research Project on Computer Science with High-Performance Computing in Nagoya University.' C. B. da Silva acknowledges Fundação para a ciência e Tecnologia (FCT), under grant PTDC/EMS-ENE/6129/2014. Some of numerical simulations presented in this manuscript were carried out on the high-performance computing system (NEC SX-ACE) in the Japan Agency for Marine-Earth Science and Technology. The authors acknowledge the Laboratory for Advanced Computing at University of Coimbra for providing HPC, computing and consulting resources (http://www.lca.uc.pt).

Appendix A

In this Appendix we compare how several flow variables evolve in HIT and within a TNTI layer by using results from the HIT1 and PJET simulations. The idea behind this comparison can be understood by recalling that when one moves from the irrotational into the turbulent region across the TNTI layer the local vorticity increases. Therefore, a conditional mean, made in relation to a distance from a fixed position within the TNTI layer, can be compared to a conditional mean made in relation to the local value of the enstrophy $\omega^2/2$. This allows one to compare the evolution of several flow variables across the TNTI (from the irrotational to the turbulent region) to how they evolve in homogeneous isotropic turbulence, from regions of weak local enstrophy to regions intense local enstrophy. Here the conditional averages (as function of $\omega^2/2$) used in HIT1 are denoted by $\langle\cdot\rangle_\omega$, where the average is performed over space. The evolution of the variables within the TNTI layer in PJET is with averages $\langle\cdot\rangle_I$, where the local coordinate ζ_I corresponds to a given mean enstrophy $\langle\omega^2/2\rangle_I$, which of course increases across the TNTI layer. Thus, the average $\langle\cdot\rangle_I$ plotted against $\langle\omega^2/2\rangle_I$ for the same ζ_I (in PJET) can be compared with the average $\langle\cdot\rangle_\omega$ plotted against $\omega^2/2$ for homogeneous isotropic turbulence (in HIT1). Notice that in PJET the viscous superlayer is formed at the outer edge of the turbulent region, where the enstrophy level is only slightly higher than in the non-turbulent region. In other words, in these conditional statistics the viscous superlayer and a part of the turbulent sublayer (for PJET) compare with the weak vorticity (small enstrophy) region of HIT1.

Figure 12(a) shows the averages, conditioned on enstrophy, of enstrophy diffusion and production, $\langle D_\omega\rangle_\omega$ and $\langle P_\omega\rangle_\omega$, plotted against $\omega^2/2$ (divided by its mean value $\langle\omega^2/2\rangle$) for HIT1. The diffusion term $\langle D_\omega\rangle_\omega$ exhibits negative and positive values for large and small values of $\omega^2/2$, respectively, which indicates that the enstrophy is transferred from regions of large $\omega^2/2$ to regions with small $\omega^2/2$, as expected. On the other hand, the production term $\langle P_\omega\rangle_\omega$ is close to 0 for small $\omega^2/2$, but rapidly increases with the enstrophy for large $\omega^2/2$, naturally expressing the dependence of the enstrophy production $P_\omega = \omega_i S_{ij}\omega_j$ on the enstrophy magnitude. Figure 12(b) shows $\langle D_\omega\rangle_I$ and $\langle P_\omega\rangle_I$ against $\langle\omega^2/2\rangle_I$ for PJET, where the associated ζ_I is in the range transitioning from the non-turbulent region to the turbulent sublayer of the TNTI layer. In the viscous superlayer, $\langle D_\omega\rangle_I$ is positive and increases with $\langle\omega^2/2\rangle_I$, before becoming negative within the turbulent sublayer. The production term $\langle P_\omega\rangle_I$ on the other hand is close to zero for small $\langle\omega^2/2\rangle_I$ (within the viscous superlayer), but it rapidly increases with $\langle\omega^2/2\rangle_I$ moving from the viscous superlayer to the turbulent sublayer, where the crossing between $\langle D_\omega\rangle_I$ and $\langle P_\omega\rangle_I$ taking place at the end of the viscous superlayer. This evolution of $\langle D_\omega\rangle_I$ and $\langle P_\omega\rangle_I$ in the TNTI layer is well documented in previous works, *e.g.* Taveira & da Silva (2014),

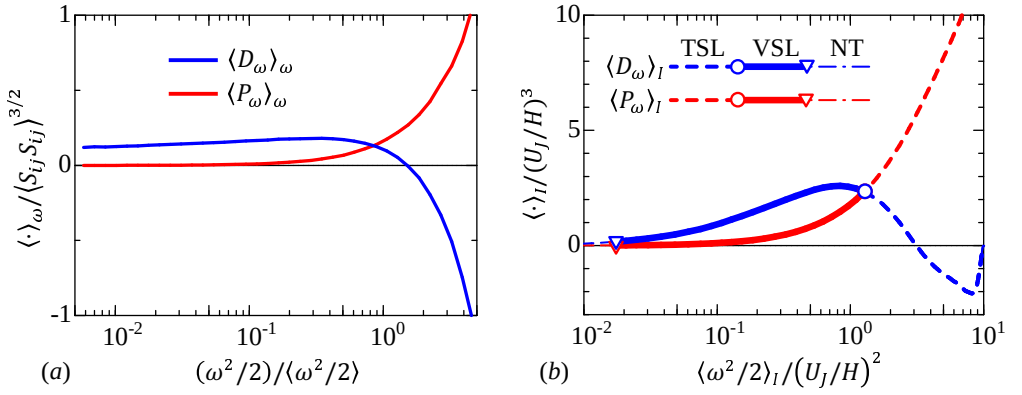

Figure 12: (a) Conditional averages on enstrophy for enstrophy diffusion and production terms, $\langle D_\omega\rangle_\omega$ and $\langle P_\omega\rangle_\omega$, for HIT1. $\langle D_\omega\rangle_\omega$ and $\langle P_\omega\rangle_\omega$ are normalized by $\langle S_{ij}S_{ij}\rangle^{3/2}$ while $\omega^2/2$ is divided by mean enstrophy $\langle\omega^2/2\rangle$. (b) $\langle D_\omega\rangle_I$ and $\langle P_\omega\rangle_I$ plotted against $\langle\omega^2/2\rangle_I$ at the same location of ζ_I within the TNTI layer in PJET. Different lines are used for the non-turbulent region (NT), viscous superlayer (VSL) and turbulent sublayer (TSL) in (b).

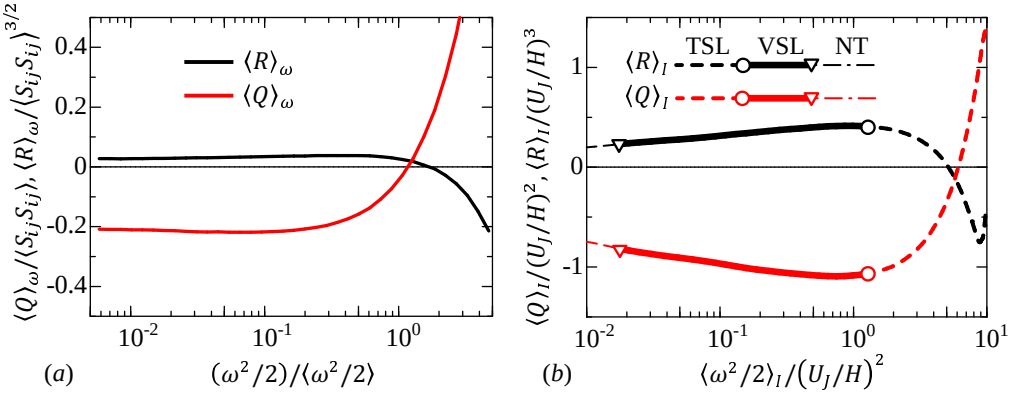

Figure 13: (a) Averages conditioned on enstrophy taken for second and third invariants of velocity gradient tensor (Q and R). (b) $\langle Q\rangle_I$ and $\langle R\rangle_I$ plotted against $\langle\omega^2/2\rangle_I$ within the TNTI layer in PJET. Different lines are used for the non-turbulent region (NT), viscous superlayer (VSL) and turbulent sublayer (TSL) in (b).

but the similarities with homogeneous isotropic turbulence are new and interesting to observe [compare figures 12 (a) and (b). The fact that regions of strong enstrophy in homogeneous isotropic turbulence are connected with the presence of intense vortices, which also somehow define the TNTI layer and can explain these similarities (Watanabe *et al.* 2017*a*). Naturally, the similarities between the TNTI layer and homogeneous isotropic turbulence end when one considers regions of very low enstrophy since while in the planar jet the enstrophy quickly tends to 0 moving into the non-turbulent region, it tends to be a small non-zero value in homogeneous isotropic turbulence, marking the regions of very weak enstrophy. This is because the non-turbulent region with $\omega^2 \approx 0$ is bounded by the outer edge of the viscous superlayer in the planar jet while low-ω^2 regions in the homogeneous isotropic turbulence can be surrounded by fluid with much higher

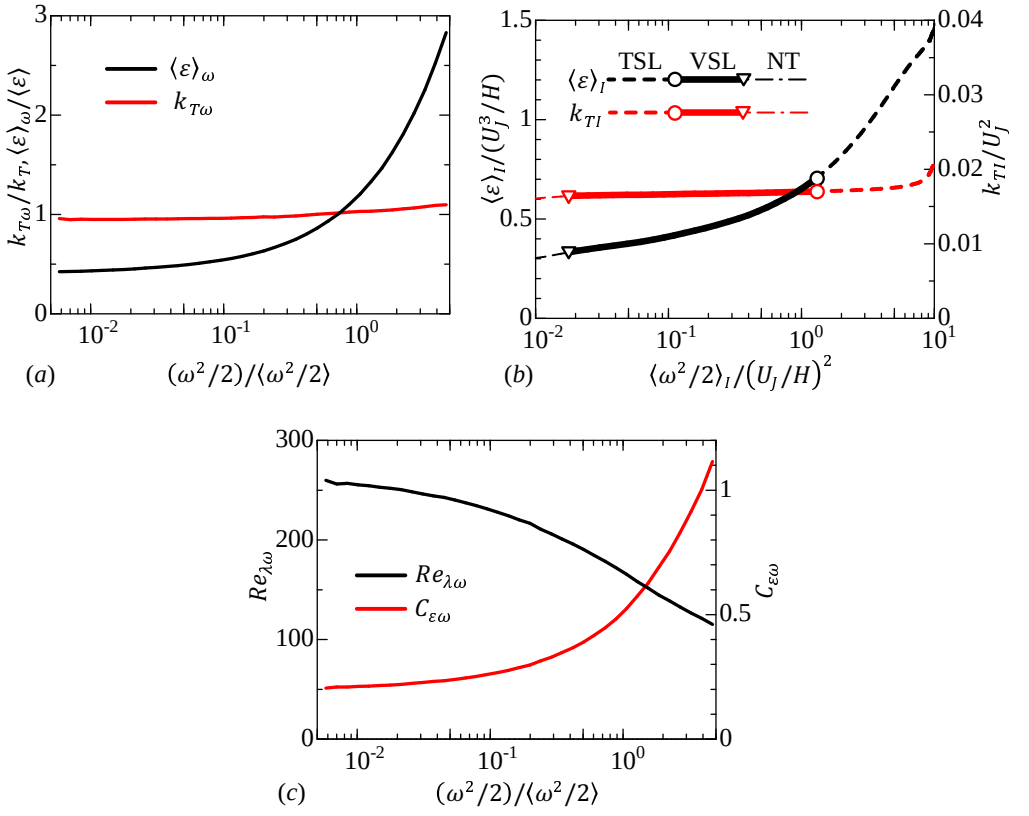

Figure 14: (a) Turbulent kinetic energy $k_{T\omega} = \langle u_j u_j\rangle_\omega/2$ and averaged kinetic energy dissipation rate $\langle\varepsilon\rangle_\omega$ computed with averages conditioned on enstrophy in HIT1. (b) Turbulent kinetic energy k_{TI} and averaged kinetic energy dissipation rate $\langle\varepsilon\rangle_I$ plotted against $\langle\omega^2/2\rangle_I$ within the TNTI layer in PJET. Different lines are used for the non-turbulent region (NT), viscous superlayer (VSL) and turbulent sublayer (TSL) in (b). (c) $Re_\lambda = (2k_{T\omega}/3)^{1/2}\lambda_\omega/\nu$ and $C_{\varepsilon\omega} = \langle\varepsilon\rangle_\omega L/(2k_{T\omega}/3)^{3/2}$ computed with conditional averages on enstrophy for HIT1, where $\lambda_\omega = (10\nu k_{T\omega}/\langle\varepsilon\rangle_\omega)^{1/2}$.

ω^2, from which enstrophy can be transferred towards the low-ω^2 regions by the viscous diffusion. Also, differences arise for large values of enstrophy, *e.g.* when $\langle D_\omega\rangle_I$ is close to 0 at $\langle\omega^2/2\rangle_I \approx 10$ in figure 12(b), while $\langle D_\omega\rangle_\omega$ in figure 12(a) decreases with $\omega^2/2$. The explanation is again simple. The average in the turbulent sublayer can contain fluid with a wide range of $\omega^2/2$, because the enstrophy is highly intermittent in the turbulent region as shown in figure 1, and averaging turbulent fluids with various values of $\omega^2/2$ results in cancellation of both positive and negative D_ω in the averaged value $\langle D_\omega\rangle_I$ for large $\langle\omega^2/2\rangle_I$ (Jahanbakhshi & Madnia 2016; Zhang *et al.* 2018). Nevertheless, it is clear that the transition from the viscous superlayer to the turbulent sublayer as observed in figure 12(b) for $\langle D_\omega\rangle_\omega$ and $\langle P_\omega\rangle_\omega$ is similar to that observed in the homogeneous isotropic turbulence.

Small-scale features of turbulent flows have been studied with the second and third invariants of velocity gradient tensor defined as $Q = (\omega_i\omega_i - 2S_{ij}S_{ij})/4$ and $R = -(S_{ij}S_{jk}S_{ki}/3 + \omega_i S_{ij}\omega_j/4)$, respectively (Ooi *et al.* 1999). Statistics of Q and R near the TNTI layer were presented in previous studies (da Silva & Pereira 2008; Watanabe

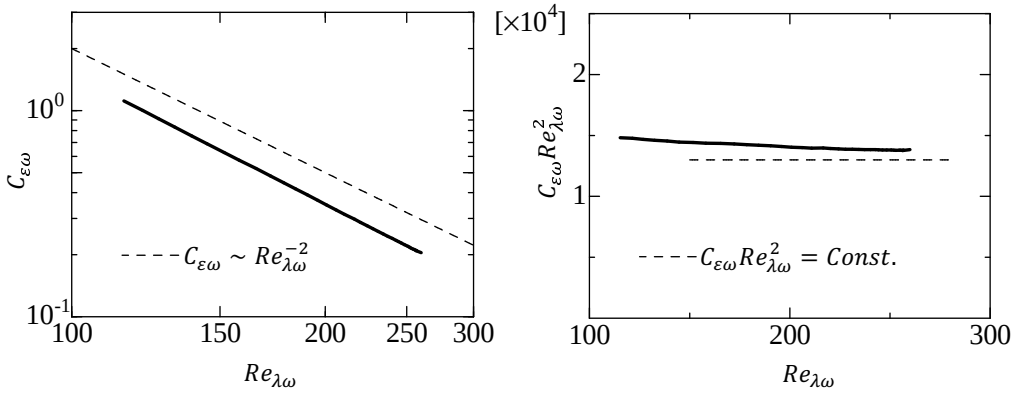

Figure 15: (*a*) $C_{\varepsilon\omega}$ and (*b*) $C_{\varepsilon\omega}Re_{\lambda\omega}^2$ plotted against $Re_{\lambda\omega}$ for HIT1.

et al. 2014; Vaghefi & Madnia 2015; Mathew *et al.* 2016; Watanabe *et al.* 2017*a*). These studies showed that $\langle Q\rangle_I < 0$ and $\langle R\rangle_I > 0$ within the viscous superlayer, changing to $\langle Q\rangle_I > 0$ and $\langle R\rangle_I < 0$ in the turbulent sublayer. Figure 13(*a*) plots $\langle Q\rangle_\omega$ and $\langle R\rangle_\omega$ against $\omega^2/2$ for HIT1 while figure 13(*b*) plots $\langle Q\rangle_I$ and $\langle R\rangle_I$ against $\langle\omega^2/2\rangle_I$ near the TNTI layer for PJET. Figure 13(*b*) confirms these trends here for the planar jet while figure 13(*a*) displays similar features for the homogeneous isotropic turbulence. This has been explained by the presence of the vortices in the homogeneous isotropic turbulence and within the TNTI layers (Watanabe *et al.* 2017*a*). In short $Q > 0$ at the vortex cores and $Q < 0$ surrounding these eddies (Davidson 2004).

Figure 14(*a*) shows the turbulent kinetic energy $k_{T\omega} = \langle u_j u_j\rangle_\omega/2$ and kinetic energy dissipation rate $\langle\varepsilon\rangle_\omega$, as a function of $\omega^2/2$ for HIT1 while figure 14(*b*) shows the results for PJET. In the two flow cases, both quantities increase with $\omega^2/2$ although the turbulent kinetic energy increases only slightly because of a very small contribution from the small scales of motions for this quantity. Using the previous data for HIT1, the turbulent Reynolds number $Re_{\lambda\omega} = (2k_{T\omega}/3)^{1/2}\lambda_\omega/\nu$ and the non-dimensional dissipation rate $C_{\varepsilon\omega} = \langle\varepsilon\rangle_\omega L/(2k_{T\omega}/3)^{3/2}$ have been computed and shown in figure 14(*c*), where $\lambda_\omega = (10\nu k_{T\omega}/\langle\varepsilon\rangle_\omega)^{1/2}$. Notice that the integral length scale L is assumed to be independent of a local value $\omega^2/2$ since L is computed from the auto-correlation function defined with two-point statistics. Similarly as in figures 8(*c*) and (*d*), $Re_{\lambda\omega}$ decreases while C_ε increases with $\omega^2/2$.

Figures 15(*a*) and (*b*) show the dependency of $C_{\varepsilon\omega}$ on $Re_{\lambda\omega}$ for HIT1. It is clear that $C_{\varepsilon\omega} \sim Re_{\lambda\omega}^{-2}$ when the statistics are computed conditioned on enstrophy. This is particularly more so at higher $Re_{\lambda\omega}$ *i.e.* $Re_{\lambda\omega} \gtrsim 200$ since $C_{\varepsilon\omega}Re_{\lambda\omega}^2$ is relatively insensitive to $Re_{\lambda\omega}$ (see figure 15(*b*)). Because higher values of $Re_{\lambda\omega}$ are associated with smaller values of $\omega^2/2$ [figure 14(*c*)] we conclude that the relation $C_{\varepsilon\omega} \sim Re_{\lambda\omega}^{-2}$ arises in regions of relatively small local $\omega^2/2$ in HIT1. This reminds us of the same relation observed previously in the viscous superlayer and the beginning of the turbulent sublayer, where the mean enstrophy is also much smaller than in the turbulent core region (see figure 9). However, as remarked by an anonymous referee, it is not certain that $C_\varepsilon \sim Re_\lambda^{-2}$ can be explained in the same manner in the two situations.

Indeed, combining the definitions of C_ε, Re_λ and λ, one can write $C_\varepsilon = 15(L/\lambda)/Re_\lambda = 15(Re_L/Re_\lambda^2)$, where $Re_L = u'L/\nu$. It follows that in HIT1, regions of roughly constant u' will display a trivial relation $C_\varepsilon \sim Re_\lambda^{-2}$, since the integral scale L is constant. It is clear that the local variations of Re_λ at these locations must come from local variations of ε

(and $\omega^2/2$). Also, from the previous figures and discussion it is clear that in these regions both ε and $\omega^2/2$ is very small, but Re_λ is high. Thus, one concludes that $C_\varepsilon \sim Re_\lambda^{-2}$ is observed in the homogeneous isotropic turbulence in regions of high Re_λ, where u' is roughly constant and where $\omega^2/2$ (and ε) are very small. This suggests that this relation is connected to the somehow 'void' regions between the eddies, or between the large clusters of eddies existing in the homogeneous isotropic turbulence. The relation $C_\varepsilon \sim Re_\lambda^{-2}$ observed in the viscous superlayer and a part of the turbulent sublayer certainly arises in a region where the level of ε and $\omega^2/2$ is very small [see figure 8(a)], and furthermore, no vortices are to be found inside these regions (which are bounded by the eddies).

REFERENCES

Alvelius, K. 1999 Random forcing of three-dimensional homogeneous turbulence. *Phys. Fluids* **11** (7), 1880–1889.

Antonia, R. A., Satyaprakash, B. R. & Hussain, A. K. M. F. 1980 Measurements of dissipation rate and some other characteristics of turbulent plane and circular jets. *Phys. Fluids* **23** (4), 695–700.

Bisset, D. K., Hunt, J. C. R. & Rogers, M. M. 2002 The turbulent/non-turbulent interface bounding a far wake. *J. Fluid Mech.* **451**, 383–410.

Borrell, G. & Jiménez, J. 2008 Properties of the turbulent/non-turbulent interface in boundary layers. *J. Fluid Mech.* **801**, 554–596.

Bos, W. J. T. & Rubinstein, R. 2017 Dissipation in unsteady turbulence. *Phys. Rev. Fluids* **2** (2), 022601.

Cleary, M. J. & Klimenko, A. Y. 2009 A generalised multiple mapping conditioning approach for turbulent combustion. *Flow, Turbul. Combust.* **82** (4), 477–491.

Corrsin, S. & Kistler, A. L. 1955 Free-stream boundaries of turbulent flows. *NACA Technical Report No. TN-1244* .

Davidson, P. A. 2004 *Turbulence: An Introduction for Scientists and Engineers*. Oxford Univ. Pr.

Deo, R. C., Mi, J. & Nathan, G. J. 2008 The influence of Reynolds number on a plane jet. *Phys. Fluids* **20** (7), 075108.

Deo, R. C., Nathan, G. J. & Mi, J. 2013 Similarity analysis of the momentum field of a subsonic, plane air jet with varying jet-exit and local Reynolds numbers. *Phys. Fluids* **25** (1), 015115.

Fox, R. O. 2003 *Computational Models for Turbulent Reacting Flows*. Cambridge Univ. Pr.

Gampert, M., Boschung, J., Hennig, F., Gauding, M. & Peters, N. 2014*a* The vorticity versus the scalar criterion for the detection of the turbulent/non-turbulent interface. *J. Fluid Mech.* **750**, 578–596.

Gampert, M., Kleinheinz, K., Peters, N. & Pitsch, H. 2014*b* Experimental and numerical study of the scalar turbulent/non-turbulent interface layer in a jet flow. *Flow, Turbul. Combust.* **92** (1-2), 429–449.

Goto, S. & Vassilicos, J. C. 2016 Unsteady turbulence cascades. *Phys. Rev. E* **94** (5), 053108.

Holzner, M., Liberzon, A., Nikitin, N., Lüthi, B., Kinzelbach, W. & Tsinober, A. 2008 A Lagrangian investigation of the small-scale features of turbulent entrainment through particle tracking and direct numerical simulation. *J. Fluid Mech.* **598**, 465–475.

Holzner, M. & Lüthi, B. 2011 Laminar superlayer at the turbulence boundary. *Phys. Rev. Lett.* **106** (13), 134503.

Jahanbakhshi, R. & Madnia, C. K. 2016 Entrainment in a compressible turbulent shear layer. *J. Fluid Mech.* **797**, 564–603.

Jahanbakhshi, R. & Madnia, C. K. 2018 Viscous superlayer in a reacting compressible turbulent mixing layer. *J. Fluid Mech.* **848**, 743–755.

Jahanbakhshi, R., Vaghefi, N. S. & Madnia, C. K. 2015 Baroclinic vorticity generation near the turbulent/non-turbulent interface in a compressible shear layer. *Phys. Fluids* **27** (10), 105105.

Kempf, A., Klein, M. & Janicka, J. 2005 Efficient generation of initial-and inflow-conditions for transient turbulent flows in arbitrary geometries. *Flow, Turbul. Combust.* **74** (1), 67–84.

Kolmogorov, A. N. 1941 On degeneration (decay) of isotropic turbulence in an incompressible viscous liquid. In *Dokl. Akad. Nauk SSSR*, , vol. 31, pp. 538–540.

Layek, G. C. & Sunita 2018 Non-kolmogorov dissipation in a turbulent planar jet. *Phys. Rev. Fluids* **3** (12), 124605.

Mathew, J., Ghosh, S. & Friedrich, R. 2016 Changes to invariants of the velocity gradient tensor at the turbulent–nonturbulent interface of compressible mixing layers. *Int. J. Heat Fluid Flow* **59**, 125–130.

Mitarai, S., Riley, J. J. & Kosaly, G. 2005 Testing of mixing models for Monte Carlo probability density function simulations. *Phys. Fluids* **17** (4), 047101.

Nagata, R., Watanabe, T. & Nagata, K. 2018 Turbulent/non-turbulent interfaces in temporally evolving compressible planar jets. *Phys. Fluids* **30** (10), 105109.

Nedić, J., Vassilicos, J. C. & Ganapathisubramani, B. 2013 Axisymmetric turbulent wakes with new nonequilibrium similarity scalings. *Phys. Rev. Lett.* **111** (14), 144503.

Ooi, A., Martin, J., Soria, J. & Chong, M. S. 1999 A study of the evolution and characteristics of the invariants of the velocity-gradient tensor in isotropic turbulence. *J. Fluid Mech.* **381**, 141–174.

Pumir, A., Shraiman, B. I & Chertkov, M. 2001 The Lagrangian view of energy transfer in turbulent flow. *EPL (Europhys. Lett.)* **56** (3), 379.

van Reeuwijk, M. & Holzner, M. 2014 The turbulence boundary of a temporal jet. *J. Fluid Mech.* **739**, 254–275.

Richardson, L. F. 1922 *Weather Prediction by Numerical Process*. Cambridge Univ. Pr.

Seoud, R. E. & Vassilicos, J. C. 2007 Dissipation and decay of fractal-generated turbulence. *Phys. Fluids* **19** (10), 105108.

da Silva, C. B. 2009 The behavior of subgrid-scale models near the turbulent/nonturbulent interface in jets. *Phys. Fluids* **21** (8), 081702.

da Silva, C. B., Hunt, J. C. R., Eames, I. & Westerweel, J. 2014 Interfacial layers between regions of different turbulence intensity. *Annu. Rev. Fluid Mech.* **46**, 567–590.

da Silva, C. B. & Pereira, J. C. F. 2008 Invariants of the velocity-gradient, rate-of-strain, and rate-of-rotation tensors across the turbulent/nonturbulent interface in jets. *Phys. Fluids* **20** (5), 055101.

Silva, T. S., Zecchetto, M. & da Silva, C. B. 2018 The scaling of the turbulent/non-turbulent interface at high Reynolds numbers. *J. Fluid Mech.* **843**, 156–179.

Sreenivasan, K. R. 1984 On the scaling of the turbulence energy dissipation rate. *Phys. Fluids* **27** (5), 1048–1051.

Takamure, K., Sakai, Y., Ito, Y., Iwano, K. & Hayase, T. 2019 Dissipation scaling in the transition region of turbulent mixing layer. *Int. J. Heat Fluid Flow* **75**, 77–85.

Taveira, R. R., Diogo, J. S., Lopes, D. C. & da Silva, C. B. 2013 Lagrangian statistics across the turbulent-nonturbulent interface in a turbulent plane jet. *Phys. Rev. E* **88** (4), 043001.

Taveira, R. R. & da Silva, C. B. 2013 Kinetic energy budgets near the turbulent/nonturbulent interface in jets. *Phys. Fluids* **25**, 015114.

Taveira, R. R. & da Silva, C. B. 2014 Characteristics of the viscous superlayer in shear free turbulence and in planar turbulent jets. *Phys. Fluids* **26** (2), 021702.

Teixeira, M. A. C. & da Silva, C. B. 2012 Turbulence dynamics near a turbulent/non-turbulent interface. *J. Fluid Mech.* **695**, 257–287.

Terashima, O., Sakai, Y., Nagata, K., Ito, Y., Onishi, K. & Shouji, Y. 2016 Simultaneous measurement of velocity and pressure near the turbulent/non-turbulent interface of a planar turbulent jet. *Exp. Therm. Fluid Sci.* **75**, 137–146.

Townsend, A. A. 1976 *The structure of turbulent shear flow*. Cambridge Univ. Pr.

Vaghefi, N. S. & Madnia, C. K. 2015 Local flow topology and velocity gradient invariants in compressible turbulent mixing layer. *J. Fluid Mech.* **774**, 67–94.

Valente, P. C., Onishi, R. & da Silva, C B. 2014 Origin of the imbalance between energy cascade and dissipation in turbulence. *Phys. Rev. E* **90** (2), 023003.

Valente, P. C. & Vassilicos, J. C. 2012 Universal dissipation scaling for nonequilibrium turbulence. *Phys. Rev. Lett.* **108** (21), 214503.

Vassilicos, J. C. 2015 Dissipation in turbulent flows. *Annu. Rev. Fluid Mech.* **47**, 95–114.

Watanabe, T., Jaulino, R., Taveira, R. R., da Silva, C. B., Nagata, K. & Sakai, Y. 2017*a* Role of an isolated eddy near the turbulent/non-turbulent interface layer. *Phys. Rev. Fluids* **2** (9), 094607.

Watanabe, T. & Nagata, K. 2016 Mixing model with multi-particle interactions for Lagrangian simulations of turbulent mixing. *Phys. Fluids* **28** (8), 085103.

Watanabe, T. & Nagata, K. 2017 Gradients estimation from random points with volumetric tensor in turbulence. *J. Comput. Phys.* **350**, 518–529.

Watanabe, T., Nagata, K. & da Silva, C. B. 2017*b* Vorticity evolution near the turbulent/non-turbulent interfaces in free-shear flows. In *Vortex Structures in Fluid Dynamic Problems*. InTech.

Watanabe, T., Riley, J. J., Nagata, K., Onishi, R. & Matsuda, K. 2018*a* A localized turbulent mixing layer in a uniformly stratified environment. *J. Fluid Mech.* **849**, 245–276.

Watanabe, T., Sakai, Y., Nagata, K., Ito, Y. & Hayase, T. 2014 Vortex stretching and compression near the turbulent/nonturbulent interface in a planar jet. *J. Fluid Mech.* **758**, 754–785.

Watanabe, T., Sakai, Y., Nagata, K., Ito, Y. & Hayase, T. 2015 Turbulent mixing of passive scalar near turbulent and non-turbulent interface in mixing layers. *Phys. Fluids* **27** (8), 085109.

Watanabe, T., da Silva, C. B. & Nagata, K. 2016*a* Multi-particle dispersion during entrainment in turbulent free-shear flows. *J. Fluid Mech.* **805**, R1.

Watanabe, T., da Silva, C. B., Nagata, K. & Sakai, Y. 2017*c* Geometrical aspects of turbulent/non-turbulent interfaces with and without mean shear. *Phys. Fluids* **29** (8), 085105.

Watanabe, T., da Silva, C. B., Sakai, Y., Nagata, K. & Hayase, T. 2016*b* Lagrangian properties of the entrainment across turbulent/non-turbulent interface layers. *Phys. Fluids* **28** (3), 031701.

Watanabe, T., Zhang, X. & Nagata, K. 2018*b* Turbulent/non-turbulent interfaces detected in DNS of incompressible turbulent boundary layers. *Phys. Fluids* **30** (3), 035102.

Wolf, M., Holzner, M., Lüthi, B., Krug, D., Kinzelbach, W. & Tsinober, A. 2013 Effects of mean shear on the local turbulent entrainment process. *J. Fluid Mech.* **731**, 95–116.

Wolf, M., Lüthi, B., Holzner, M., Krug, D., Kinzelbach, W. & Tsinober, A. 2012 Investigations on the local entrainment velocity in a turbulent jet. *Phys. Fluids* **24** (10), 105110.

Zhang, X., Watanabe, T. & Nagata, K. 2018 Turbulent/nonturbulent interfaces in high-resolution direct numerical simulation of temporally evolving compressible turbulent boundary layers. *Phys. Rev. Fluids* **3** (9), 094605.